JACS
JOURNAL OF THE AMERICAN CHEMICAL SOCIETY
pubs.acs.org/JACS
Article

Correlating Kinetics to Cyclability Reveals Thermodynamic Origin of Lithium Anode Morphology in Liquid Electrolytes

David T. Boyle, Sang Cheol Kim, Solomon T. Oyakhire, Rafael A. Vilá, Zhuojun Huang, Philaphon Sayavong, Jian Qin, Zhenan Bao,* and Yi Cui*

Cite This: J. Am. Chem. Soc. 2022, 144, 20717−20725
Read Online
ACCESS | Metrics & More | Article Recommendations | Supporting Information

ABSTRACT: The rechargeability of lithium metal batteries strongly depends on the electrolyte. The uniformity of the electroplated Li anode morphology underlies this dependence, so understanding the main drivers of uniform plating is critical for further electrolyte discovery. Here, we correlate electroplating kinetics with cyclability across several classes of electrolytes to reveal the mechanistic influence electrolytes have on morphology. Fast charge-transfer kinetics at fresh Li−electrolyte interfaces correlate well with uniform morphology and cyclability, whereas the resistance of Li^+ transport through the solid electrolyte interphase (SEI) weakly correlates with cyclability. These trends contrast with the conventional thought that Li^+ transport through the electrolyte or SEI is the main driver of morphological differences between classes of electrolytes. Relating these trends to Li^+ solvation, Li nucleation, and the charge-transfer mechanism instead suggests that the Li/Li^+ equilibrium potential and the surface energy—thermodynamic factors modulated by the strength of Li^+ solvation—underlie electrolyte-dependent trends of Li morphology. Overall, this work provides an insight for discovering functional electrolytes, tuning kinetics in batteries, and explaining why weakly solvating fluorinated electrolytes favor uniform Li plating.

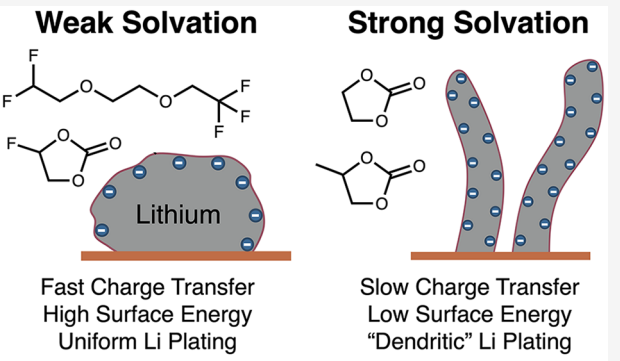

INTRODUCTION

Rechargeable lithium metal batteries could help electrify high-energy applications such as electric passenger cars, aeronautics, and long-range trucking.[1] However, insufficient Coulombic efficiency (CE), the ratio of Li output to Li input during discharge and charge, respectively,[2] remains a key bottleneck limiting the widespread adoption of Li metal anodes. Electrolyte chemistry strongly impacts the CE of Li, so engineering and discovery of electrolytes has been a decades-long focus.[3−8] In general, four common classes of electrolytes have emerged for Li metal anodes: carbonates, fluorinated carbonates, ethers, and fluorinated ethers (Figure 1A). The CE of Li in each class is closely related to the morphology of electroplated Li during charging, with fluorinated solvents that weakly solvate Li^+ generally plating larger grains of Li and having higher CE (Figure 1B,C). Uniform morphology mitigates the main causes of anode degradation—corrosive reactions with the electrolyte and electrical disconnection of Li during battery discharge.[9,10] Despite these two identified causes, the mechanistic basis for distinct morphologies across classes of electrolyte remains poorly understood. Instead, identification of F-/anion-rich passivation film on Li called the solid electrolyte interphase (SEI) has been a primary driver of electrolyte design.[6] Further efforts in electrolyte discovery and engineering would benefit from identification of the underlying mechanism of morphological control across electrolyte classes.

Correlating electroplating kinetics to cyclability is one potential strategy for elucidating the main drivers of lithium morphology. Relationships between the electrolyte, electroplating kinetics, and morphology are well established for several non-reactive metals;[11,12] however, the literature is mixed for reactive Li metal. Reports on no correlation,[6] positive correlation,[13−16] and negative correlation[17−20] between faster interfacial electroplating kinetics and cyclability all exist. One reason for these discrepancies is that the reactivity of Li is often neglected in kinetic analysis. Most electrolytes react with Li and form a nanometers-thick and ionically conductive compact SEI that directly contacts Li.[21,22] Depending on charging rate, electroplating can occur at either buried Li−SEI interfaces or fresh Li−electrolyte interfaces when the SEI fractures, with each pathway having distinct electroplating kinetics.[23−25] Resolving the kinetics of these two pathways

Received: August 2, 2022
Published: November 1, 2022

https://doi.org/10.1021/jacs.2c08182
J. Am. Chem. Soc. 2022, 144, 20717−20725

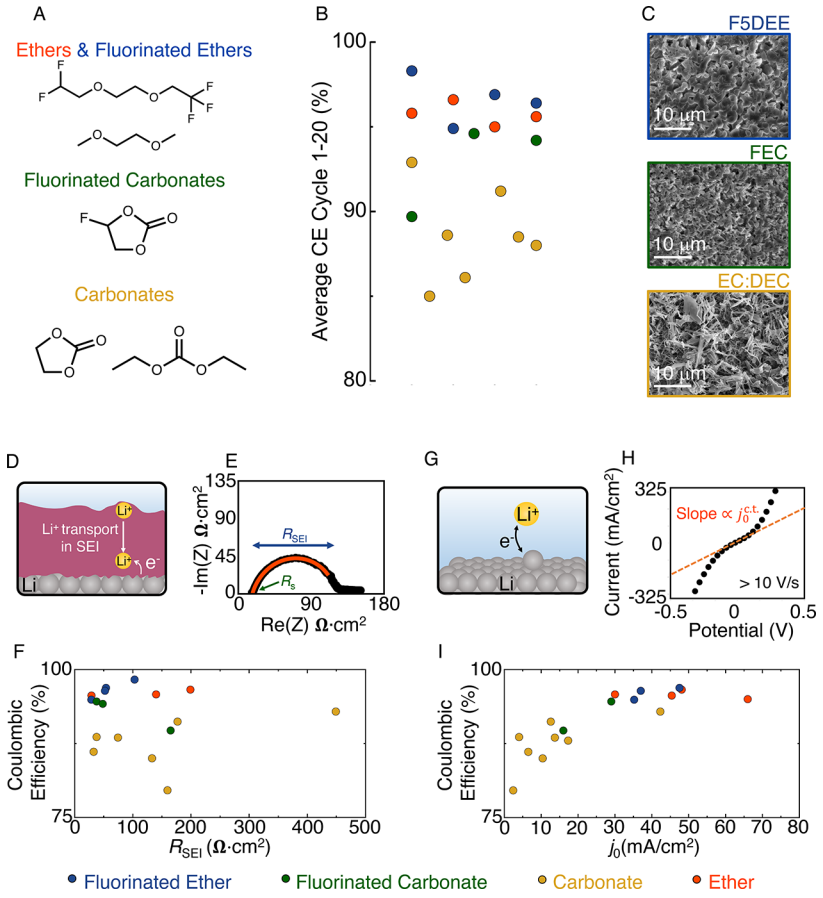

Figure 1. Correlation of electroplating kinetics to the cyclability of Li anodes. (A) Scheme of the four classes of electrolyte solvents commonly used for lithium batteries. (B) CE of about 20 select electrolytes showing the trend in CE vs class of electrolytes. (C) SEM images of Li plated in three representative electrolytes (1 mA/cm^2, 1 mA h/cm^2): 1 M $LiPF_6$ in EC/DEC, 1 M LiFSI in FEC, and 1 M LiFSI in F5DEE, showing the trend in morphology with the class of electrolytes and CE. (D) Schematic of the first electroplating pathway at the buried Li−SEI interface, where Li^+ transport is rate limiting. (E) Representative EIS spectrum of a Li||Li symmetric cell, indicating how R_{SEI} and R_S are calculated. (F) Relationship between R_{SEI} and CE of Li anodes across several classes of electrolytes. The dashed line is a guide to the eye, and it shows a lack of a clear trend. (G) Schematic of the second electroplating pathway at the Li−electrolyte interface when the SEI fractures. (H) Representative voltammogram of a piece of the transient voltammetry measurements, indicating how $j_0^{c.t.}$ is calculated. (I) Relationship between $j_0^{c.t.}$ and CE of Li anodes across several electrolytes. Data in (F,I) adapted in part from ref[23] with permission. Copyright 2020 American Chemical Society. The dashed line is a guide to the eye.

across each class of electrolytes is thus key to establish the relationship between kinetics and Li morphology.

Here, we use transient ultramicroelectrode voltammetry and electrochemical impedance spectroscopy (EIS) to correlate the kinetics of each electroplating pathway with cyclability. The correlations contrast with common models of electroplating that focus on the balance of interfacial kinetics and ion transport, so we instead propose that the strength of Li^+ solvation in distinct electrolytes thermodynamically impacts the preference for dendritic or uniform morphology. Analysis of Li^+ solvation, Li nucleation, and the electroplating mechanism in a variety of electrolytes support this model. The work provides a mechanistic basis for the dependence of electroplated Li morphology on the electrolyte and an insight into how electrolyte engineering can tune electrochemical kinetics.

RESULTS AND DISCUSSION

Correlation of Cyclability with Electroplating Kinetics. Consideration of two distinct electroplating pathways and kinetic parameters is necessary to correlate the interfacial $Li^+ + e^- \rightarrow Li^0$ kinetics with cyclability. First is electroplating at the buried Li−SEI interface (Figure 1D). In this scenario, Li^+ transport through the SEI is the major component of the interfacial impedance (i.e., electroplating kinetics).[6,9,23,24] The interfacial resistance (R_{SEI}) parameterizes the kinetics of this pathway and is easily measurable with EIS of symmetric Li||Li cells.[23,24] Second is electroplating at fresh Li−electrolyte interfaces, which can happen when the SEI fractures during fast volume expansion of electroplated Li.[23,24] For this pathway, interfacial charge transfer at fresh Li−electrolyte interfaces is the key electroplating reaction (Figure 1G). Recently, our group developed a transient cyclic voltammetry method using ultramicroelectrodes to measure charge-transfer kinetics at fresh Li−electrolyte interfaces.[23] The low overpotential slope of the voltammogram can be directly related to the intrinsic exchange current density of charge transfer ($j_0^{c.t.}$)—the equivalent of a standard rate constant—at fresh Li−electrolyte interfaces (Figures 1H, S2, and S3).[23] The electroplating kinetics of each pathway parameterized by R_{SEI} for ion transport through SEI and $j_0^{c.t.}$ for charge transfer at fresh Li−electrolyte interfaces can then be related to the CE of Li across each class of electrolytes.

https://doi.org/10.1021/jacs.2c08182
J. Am. Chem. Soc. 2022, 144, 20717−20725

Plotting CE as a function of $j_0^{c.t.}$ and R_{SEI} (Figure 1F,I) reveals that CE is more strongly correlated with $j_0^{c.t.}$ than R_{SEI}. We previously reported that weaker solvation or anion binding to Li^+ increases $j_0^{c.t.}$,[23] so this trend is empirically consistent with the growing consensus that weakly solvating electrolytes plate Li uniformly with higher CE.[3−8] (The characteristics of electrolytes with fast $j_0^{c.t.}$ are verified in more detail below.) However, the mechanism underlying the relationship between weak solvation and beneficial morphology still needs clarification. In the following, we discuss the potential causes of this trend and ultimately propose that more positive Li/Li^+ equilibrium potential ($E_{eq.}^{Li/Li+}$) and higher surface energies of Li with weakly solvating electrolytes underlie uniform plating.

Classical models of metal deposition are commonly used to relate the electroplating kinetics to the morphology of non-reactive metals. Such models generally predict that slow interfacial kinetics relative to transport in the electrolyte can minimize gradients of Li^+ concentration and favor uniform morphology.[26,27] Dimensionless analysis of the interfacial kinetics measured in Figure 1F,I relative to ion transport in the electrolyte shows that our results contrast with these predictions (Figure 2). In the first electroplating pathway,

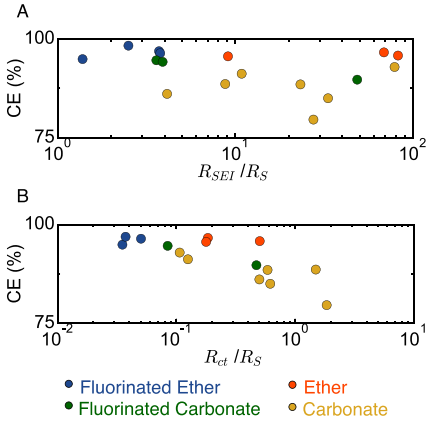

Figure 2. Comparison of classical theories of metal plating with the performance of electrolytes using dimensionless analysis. (A) Relationship between electrolyte CE and R_{SEI}/R_S. (B) Relationship between electrolyte CE and $R_{c.t.}/R_S$.

where the interfacial resistance R_{SEI} can be compared to the electrolyte solution resistance (R_s, Figure 1E), no correlation is observed between R_{SEI}/R_S and the CE (Figure 2A). Conversion of $j_0^{c.t.}$ (for charge transfer at fresh Li−electrolyte interfaces) to a resistance ($R_{c.t.}$) is done via

$$R_{c.t.} = \frac{RT}{Fj_0^{c.t.}} \tag{1}$$

where R is the standard gas constant, T is the temperature, and F is the Faraday constant,[28] also showing that $R_{c.t.}/R_s$ is negatively correlated with CE (Figure 2B). Because there is no trend in R_{SEI}/R_S (Figure 2A) and many of the fluorinated and ether electrolytes with the highest CE are in regimes with lower $R_{c.t.}/R_S$ (Figure 2B), distinct ionic conductivities or gradients of Li^+ concentration can be ruled out as the main driver of morphological differences between classes of electrolytes. This finding is consistent with the fact that some fluorinated ether electrolytes have an order of magnitude lower conductivities than carbonates but still plate Li uniformly and have high CE.[29] Our finding is also reasonable since typical battery charging/discharging current densities studied in the literature below about 1 mA/cm^2 do not necessarily create the large Li^+ concentration gradients needed to initiate the fractal growth of Li at Sand's time when the Li^+ surface concentration reaches 0. Within a class of electrolyte, however, ionic conductivity will influence the morphology during fast charging.[3] Overall, this analysis suggests that simulations applying models of non-reactive metal plating should be used cautiously to describe Li plating.

Because classical models of metal plating contrast with our results, we next consider the potential role of the SEI. Weakly solvating electrolytes, which are generally fluorinated ethers and carbonates, form SEIs that are rich with F-/anion-based components.[3−8] However, the relationship between such SEI chemistry and Li morphology remains unclear.[5] Electrolytes with similar degrees of fluorination and SEI chemistry can give notably distinct cyclabilty.[30,31] A recent study also showed that the choice of electrolyte is more important than whether an artificial LiF SEI is preformed on Li.[32] Furthermore, preformation of the F-rich SEI with a weakly solvating electrolyte does not necessarily improve subsequent Li plating if the electrolyte is switched to a low CE chemistry.[32] Lack of a strong correlation of R_{SEI} with CE is consistent with these findings (Figure 1F), where similar SEI chemistries may be expected to approach similar R_{SEI}. This lack of trend also suggests that fast ion transport through the SEI is not broadly responsible for uniform plating. While it is plausible that SEI characteristics such as mechanical strength could influence the morphology, we ask whether an alternative driving force besides the characteristics of the SEI alone may underlie the differences of Li morphology across the classes of electrolytes and complement the strong passivity of LiF-rich SEI.

Mechanism of Morphological Control in Liquid Electrolytes. One alternative explanation for our results is that weak solvation of Li^+, which increases $j_0^{c.t.}$, also positively shifts $E_{eq.}^{Li/Li+}$, creating more favorable conditions for uniform morphology and high CE. Although it is seldom considered in the battery literature,[33,34] $E_{eq.}^{Li/Li+}$ depends on the free energy of solvated Li^+. Electrolytes that weakly solvate Li^+ shift $E_{eq.}^{Li/Li+}$ to more positive values.[8] This shift has two effects that can impact Li morphology. First, because the potential of zero charge (ϕ_{pzc}) does not vary much with solvent and Li has a negative surface charge density (σ) at battery-relevant potentials, electrolytes with weaker solvation of Li^+ will have a less-negative σ than those with strong solvation.[33,34] Recent density functional theory studies showed that less-negative σ minimizes the surface charge fluctuations and prevents dendrite growth caused by the concentration of negative charge at dendrite tips.[33] Second, more positive $E_{eq.}^{Li/Li+}$ can also create a thermodynamic driving force for more uniform plating through modulation of the surface energy (γ) via the classical electrocapillary equation

$$\gamma(E) - \gamma(E_{pzc}) = -\int_{E_{pzc}}^{E} \sigma(E')\mathrm{d}E' \tag{2}$$

where E is the electrode potential.[28,33,34] Surface energy is maximized at E_{pzc} because there is zero excess charge density on Li. As $E_{eq.}^{Li/Li+}$ moves more negatively from E_{pzc}, the surface energy decreases and it becomes more thermodynamically

https://doi.org/10.1021/jacs.2c08182
J. Am. Chem. Soc. 2022, 144, 20717−20725

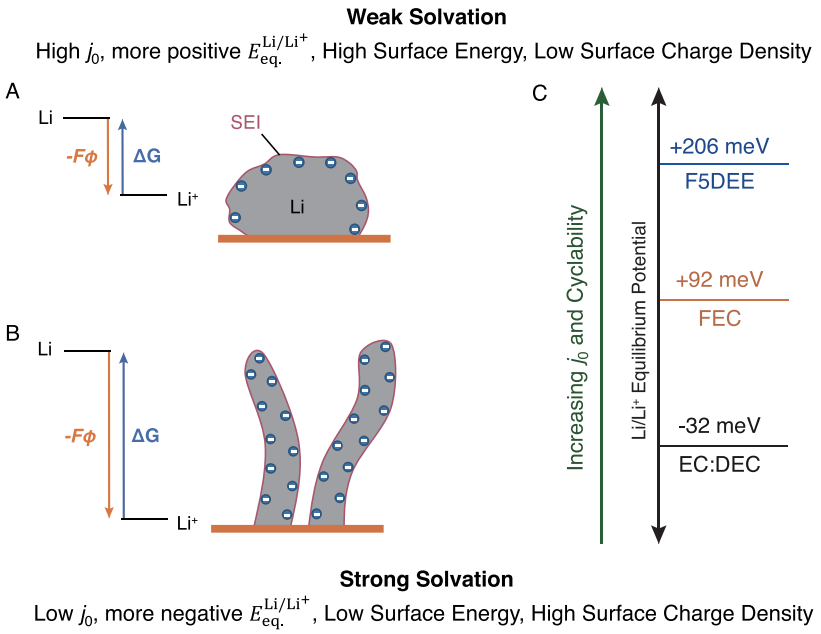

Figure 3. Impact of Li^+ solvation on the Li/Li^+ equilibrium potential, Li surface energy, and Li morphology. (A) Schematic of the proposed model where weak solvation in electrolytes with high $j_0^{c.t.}$ induces higher surface energies of Li and favors electroplating of bulky uniform Li morphology. (B) Schematic of the opposite case where strong solvation favors high surface area plating. (C) Comparison of $E_{eq.}^{Li/Li+}$ obtained from potentiometric measurements of solvation energy in three representative electrolytes: 1 M $LiPF_6$ in EC/DEC, 1 M LiFSI in FEC, and 1.2 M LiFSI in F5DEE. The reference potential at 0 V is 1 M LiFSI in DEC as used in our previous report.[8]

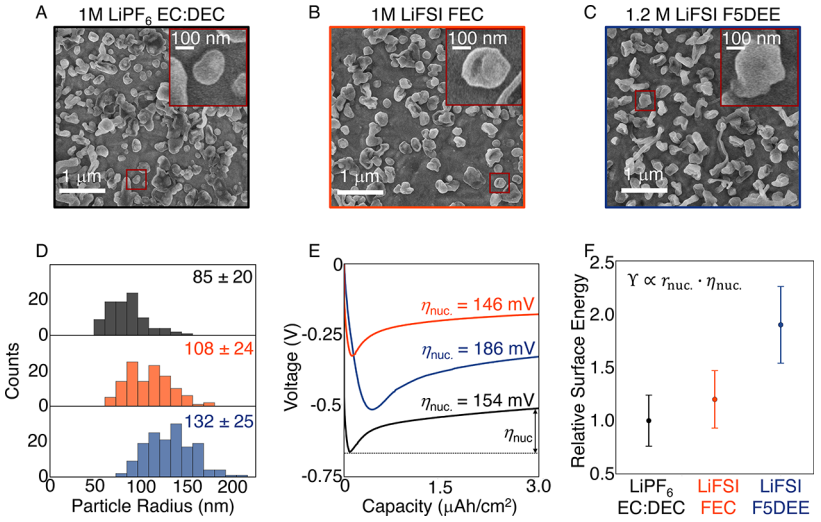

Figure 4. Electrolyte-dependent nucleation and growth of Li. (A) Representative SEM image of 0.03 mA h/cm^2 of electroplated Li in $LiPF_6$ (EC/DEC), (B) LiFSI (FEC), and (C) LiFSI (F5DEE) showing the particle size of Li. A representative particle near the average radius is highlighted in the red box and magnified in the inset. (D) Histogram of Li particle size measured from SEM images. Colors correspond to the outline of the SEM images for each electrolyte in (A–C). (E) Voltage profile of the initial nucleation stage used to calculate $\eta_{nuc.}$. (F) Relative surface energies calculated from the particle size in (D) and $\eta_{nuc.}$ in (E).

favorable to plate high surface areas that dilute the negative σ. Essentially, eq 2 states that more positive $E_{eq.}^{Li/Li+}$ with weakly solvating electrolytes will increase the surface energy and thermodynamically favor uniform Li plating (Figure 3A). In contrast, electrolytes that strongly solvate Li^+ lower the surface energy and favor the growth of high surface area "dendritic" Li to dilute the more negative surface charge density (Figure 3B). In the following, we will characterize the strength of Li^+ solvation and the influence of surface energy on Li morphology to support these hypotheses.

Potentiometry of symmetric Li|Li cells with asymmetric electrolytes provides a simple method to characterize the strength of Li^+ solvation and the relative $E_{eq.}^{Li/Li+}$ in select electrolytes.[8] Figure 3C shows the relative $E_{eq.}^{Li/Li+}$ with three representative electrolytes of the trend shown in Figure 1I (Table S2) that span the carbonate, fluorinated carbonate, and fluorinated ether classes: $LiPF_6$ in ethylene carbonate:diethyl carbonate (EC/DEC), lithium bis(fluorosulfonyl)imide (LiFSI) in fluoroethylene carbonate (FEC), and LiFSI in a fluorinated derivative of 1,2-diethoxyethane (F5DEE).[3] Con-

https://doi.org/10.1021/jacs.2c08182
J. Am. Chem. Soc. 2022, 144, 20717–20725

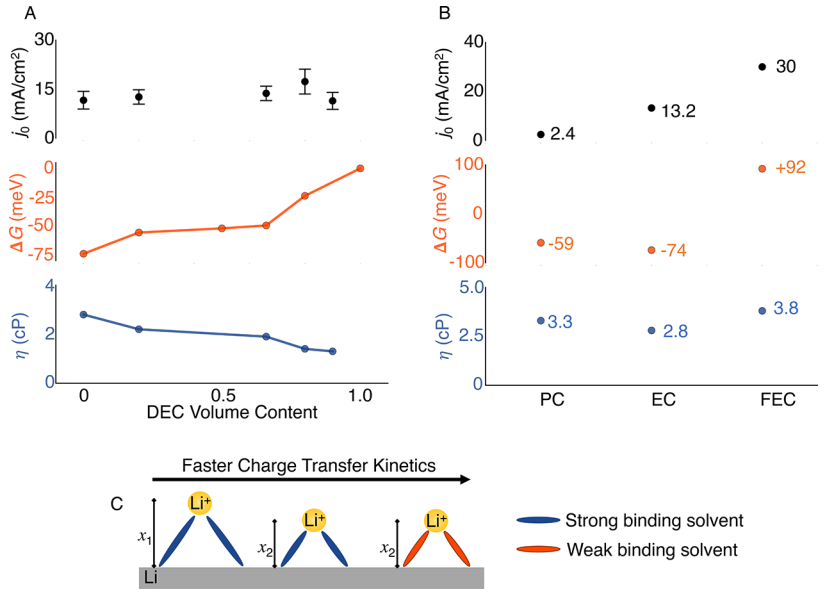

Figure 5. Molecular factors influencing the charge-transfer kinetics. (A) Relationship of $j_0^{c.t.}$, free energy of solvated Li^+, and viscosity η to the volume fraction of DEC in 1 M LiFSI (EC/DEC) electrolyte. (B) Dependence of $j_0^{c.t.}$ and free energy of solvated Li^+ bulk electrolyte and viscosity on cyclic carbonate electrolytes: 1 M LiFSI in PC, EC, and FEC. (C) Schematic indicating how changes of the interfacial structure and binding energy of the solvent to Li^+ influence $j_0^{c.t.}$. The x_1 and x_2 indicate the distinct distances of Li^+ from the surface in PC, EC, and FEC electrolytes.

sistent with our findings in a previous report,[8] electrolytes with higher CE have weaker solvation and a more positive $E_{eq.}^{Li/Li+}$. The F5DEE electrolyte is 248 meV more positive than the EC/DEC carbonate electrolyte commonly used in Li-ion batteries and 114 meV more positive than the FEC electrolyte. This result and eq 2 suggest that the weakly solvating and high CE fluorinated electrolyte, F5DEE, has the most positive σ, minimizing the surface charge fluctuations and increasing the surface energy. Therefore, it should favor uniform morphology. Opposite results are expected for the low CE and strongly solvating carbonate-based electrolyte. Ex situ scanning electron microscopy (SEM) images of electrodeposited Li in Figure 1C match these expectations: nanoscopic filaments, micron-scale grains, and an intermediate morphology are observed in EC/DEC, F5DEE, and FEC, respectively. This finding of weaker solvation leading to a more uniform morphology is consistent with our proposal in Figure 3 and complements the current understanding that the F-rich SEI is beneficial for Li anodes.

Evaluation of the earliest stages of Li plating on a copper current collector also confirms that surface energy can be a primary influence on Li morphology. According to the classical theories of nucleation, surface energy is related to the critical radius of nucleation ($r_{crit.}$) and overpotential of nucleation ($\eta_{nuc.}$) via

$$\Upsilon = \frac{r_{crit.} F \eta_{nuc.}}{2V_M} \quad (3)$$

where F is the Faraday constant and V_M is the molar volume of Li.[35,36] Measurement of $\eta_{nuc.}$ and particle size thus provides a simple means to compare the surface energies of Li in different electrolytes. Figure 4A–C shows representative SEM images of 0.03 mA h/cm^2 Li plated at 1 mA/cm^2 on Cu used to measure the Li particle size. Measurements of individual and separable Li particles with each electrolyte using SEM images shows that the particle radius increases from about 85 nm with EC/DEC to 132 nm in F5DEE with FEC having an intermediate 108 nm (Figures 4D and S5–S8). Representative particles near the average radius are shown as insets in Figure 4A–C and highlighted within the red box. The nucleation overpotential can be calculated from the voltage profiles shown in Figure 4E. Using particle radii as a rough estimation of the trend of $r_{crit.}$ in each electrolyte and $\eta_{nuc.}$ with eq 3 shows that the relative surface energy increases from EC/DEC < FEC < F5DEE (Figure 4F)—consistent with our proposal. We report the estimates for the relative surface energies, as the true $r_{crit.}$ is likely much smaller: previously reported consistency of estimates using particle size as a proxy for the true $r_{crit.}$ with classical nucleation theory suggests that this approach is reliable.[35,36] The key insight here is that Υ of the Li anode–electrolyte interface is the main driver of early-stage Li morphology. When the current density is varied, $\eta_{nuc.}$ alone provides a predictor of particle size,[35,36] but when the electrolyte changes, high Υ can overcome the effect of large $\eta_{nuc.}$ and favor plating of larger particles. The F5DEE electrolyte most clearly demonstrates this point. It gives the best morphology but requires the largest $\eta_{nuc.}$. We note that alternative explanations that F or anion-rich SEI also increases the interfacial energy cannot be fully ruled out.[37] However, as mentioned above, the SEI of similar chemistry or an artificially grown LiF SEI has not necessarily led to morphological improvements.[30–32] The key message here is not that SEI chemistry and structure are unimportant. Rather, it is that weak solvation of Li^+ in high-performance electrolytes such as fluorinated ethers can shift $E_{eq.}^{Li/Li+}$ positively and increase the surface energy via eq 2, complementing the benefits of F- or anion-rich SEI for preventing SEI fracture[24] and slowing SEI growth.[9]

Molecular Factors Influencing Charge-Transfer Kinetics. To further support our proposal in Figure 3, we provide an additional insight into the characteristics of solvents with fast $j_0^{c.t.}$. As mentioned above, we previously reported that stronger solvation of Li^+ lowers the free energy of Li^+[8] and can slow $j_0^{c.t.}$.[23] To fully verify that electrolytes with the weakest solvation also have fast $j_0^{c.t.}$ and high surface energy,

https://doi.org/10.1021/jacs.2c08182
J. Am. Chem. Soc. 2022, 144, 20717–20725

deconvolution of the effects of viscosity, ion pairing, and the strength of solvent binding to Li^+ on $j_0^{c.t.}$ is necessary. Unavailable in our previous report,[23] the potentiometric measurement in Figure 3,[8] which directly probes solvation strength with more reliability than solvent properties such as donor numbers or dielectric constants, and viscosity measurements now make deconvolution feasible. This analysis will ultimately verify that weak solvation is a major determinant of higher $j_0^{c.t.}$. Verification supports the above findings that fluorinated electrolytes with the highest CE have more positive $E_{eq.}^{Li/Li+}$ and higher surface energy, while providing an additional insight into how the kinetics of reactions in batteries are tunable with electrolyte chemistry.

First, we demonstrate that viscosity is not a major influence on $j_0^{c.t.}$ by measuring $j_0^{c.t.}$ as a function of DEC fraction in LiFSI EC/DEC $1 - x$:x by volume. Increasing the DEC content in the electrolyte systematically lowers the viscosity of the electrolyte (Figure 5A). The kinetic prefactor of some electrochemical reactions is thought to be proportional to the electrolyte viscosity,[28] but Figure 5B shows a weak relationship between $j_0^{c.t.}$ and the volume content of DEC. Lack of a trend is also not caused by a counteracting strengthening of Li^+ solvation (Figure 5A), as the free energy of Li^+ becomes less negative with increasing DEC content. However, the free energy difference from LiFSI in EC to EC/DEC 1:4 only spans about 50 meV or about 2 k_BT. This finding suggests that the bulk characteristics of the electrolyte alone (viscosity and solvation strength) may not be fully sufficient to understand the trends of $j_0^{c.t.}$. Another potential influence on $j_0^{c.t.}$ is the interfacial structure. Theories of similar reactions to Li electroplating such as Ag deposition,[38] ion-coupled electron transfer,[39] and proton-coupled electron transfer[40] predict that the rate depends on both the strength of solvation and the distance of the solvated ion from the electrode. Preferential solvation or distinct free energies at the interface could also influence$j_0^{c.t.}$. In binary EC/DEC solvents, molecular dynamics simulations have shown that EC preferentially solvates Li^+ at the interface,[41,42] which may explain the weak dependence of $j_0^{c.t.}$ on DEC content, for example.

To evaluate the balance between interfacial structure and strength of solvation without the confounding factor of preferential solvation and verify explicitly that weak solvation will increase $j_0^{c.t.}$, we investigate $j_0^{c.t.}$ in a select series of similar cyclic carbonate electrolytes—1 M LiFSI in EC, FEC, and propylene carbonate (PC) (Figure 5B). The similar characteristics of these solvents can help deconvolute the impact of solvation energy and distance.

First, we compare 1 M LiFSI in EC and PC. Despite only 25 meV or 1 k_BT difference in the free energy of solvated Li^+ and similar viscosities, $j_0^{c.t.}$ differs by an order of magnitude (13.2 vs 2.4 mA/cm^2, respectively) (Figure 5B). The key difference between solvents is the extra methyl group on PC. Molecular dynamics simulations have shown that Li^+ retains their solvation structure in the double layer near $E_{eq.}^{Li/Li+}$ with cyclic carbonates,[42] so the additional methyl group likely increases the distance between solvated Li^+ and electrode. Consistent with the theories of Ag deposition,[38] the larger distance Li^+ traverses through the transition state slows the charge-transfer reaction.

A distinct situation that is more critical for the discussion of this paper is apparent when comparing the EC and FEC electrolyte. FEC only differs from EC by the replacement of a C−H bond with a C−F bond. Hence, the position of a solvated Li^+ in the double layer is likely similar, but Li^+ in FEC has a free energy 164 meV or about 7 k_BT more positive than EC (Figure 5B). The substantially weaker solvation of Li^+ in FEC results in a much faster $j_0^{c.t.}$ (30 vs 13.2 mA/cm^2, respectively). Bulk viscosity values in Figure 5C still cannot explain the change of $j_0^{c.t.}$. Many of the electrolytes including those compared in Figure 3 fall into similar ranges of viscosity (F5DEE is about 3.3 cP[3]), so viscosity differences are still ruled out as the main factor affecting $j_0^{c.t.}$ and its trend with CE. This comparison verifies that large differences between the free energy of Li^+ are a major factor determining $j_0^{c.t.}$. Further discussion of the charge-transfer mechanism is included in our previous paper,[23] but the key point here is that both the free energy of solvated ions/reactants and the interfacial structure of the double layer can influence the kinetics of charge-transfer reactions in batteries.[43,44]

Ultimately, the extremely weak solvation of Li^+ in the fluorinated ether electrolytes with the best cyclability (Figure 1I and Table S2)—typically 300−400 meV more positive than carbonate electrolytes[3,8]—supports our proposal that solvation free energy correlates with the surface energy of Li. Although resolving the exact interfacial structure of this class of electrolyte experimentally is challenging, such weak solvation will increase $j_0^{c.t.}$ and the surface energy, favoring plating of bulky low surface area Li and high CE. This insight is consistent with the findings in recent work that weak solvation correlates with high CE[8] and adds a complementary picture to the current understanding of the benefits of F or anion-rich SEI. A promising strategy for further electrolyte engineering may thus be to design electrolyte formulations (e.g., solvents, co-solvents, and additives) that weaken solvation strength without sacrificing the solubility of lithium salts and ionic conductivity.

CONCLUSIONS

This study relates electroplating kinetics to Li anode rechargeability to understand the relationship between liquid electrolyte chemistry and the electroplated Li morphology. We find that electrolytes with weak solvation and fast interfacial charge transfer at fresh Li−electrolyte interfaces have higher CE. The resistance of Li^+ transport through the SEI, however, weakly correlates with CE. This finding contrasts with conventional thought that differences in the ionic conductivity of the electrolyte/SEI are the primary factors underlying the morphological dependence of Li on different classes of electrolytes. Instead, our results suggest that weak solvation shifts the Li/Li^+ equilibrium potential positively and increases the surface energy of Li to favor uniform plating. This finding helps explain why fluorinated electrolytes generally produce more favorable Li morphology and cyclability. The fact that weaker solvation tunes the thermodynamic preference for high or low surface area plating complements current understanding that F-/anion-rich SEI formed in weakly solvating electrolytes helps prevent SEI breakdown and corrosion. Notably, a complete quantitative connection between Li morphology and electrolyte characteristics under all charging conditions still requires more comprehensive modeling that includes SEI fracture and ionic conductivity of the SEI/electrolyte, which become increasingly important during fast charging. However, the general trend we identify can help screen electrolyte candidates at early stages. Our suggested roadmap for electrolyte discovery is thus to screen fluorinated solvents

https://doi.org/10.1021/jacs.2c08182
J. Am. Chem. Soc. 2022, 144, 20717−20725

that further push weak solvation of Li^+. Because weak solvation may also lower the ionic conductivity though, implementation of complementary strategies that improve the ionic conductivity, such as separator modifications or addition of co-solvents/additives that improve Li^+ transport, will also be necessary to meet fast charging and discharging goals. Last, this work highlights how molecular characterization of double layers and surface tensions in lithium batteries is needed and could provide an insight for tuning the morphology of electroplated metals and battery kinetics generally.

METHODS

Transient Cyclic Voltammetry. The method described in detail previously[23] was used to measure $j_0^{c.t.}$. Home-built tungsten disc ultramicroelectrodes (UMEs) were built by flame-sealing a 12.5 μm radius wire into a borosilicate glass. Prior to each measurement, the electrodes were polished with 0.3 and 0.1 μm diamond lapping pads, subsequently rinsed with deionized water and acetone, and finally dried briefly in an oven. Transient cyclic voltammetry measurements were run in an argon-filled glovebox in a beaker cell. The UME was the working electrode, and Li metal (1−2 cm^2) was the counter/reference electrode. Previously, we also used a three-electrode configuration, but use of a two-electrode system is also sufficient given the low nominal currents. For the UME measurements, iR_u drop was measured with EIS at 100 kHz and compensated with positive feedback. A 16-channel electrochemical workstation (VMP3, Biologic Science Instruments) was used to sweep the potential of the UME linearly from an open-circuit voltage (OCV) of about 3 V to about −1 to −2 V versus $E_{eq.}^{Li/Li+}$ at a scan rate of 10−200 V/s and back to the OCV. Scan rates were chosen to be consistent with our previous report to approach the range of kinetic irreversibility and ensure that the voltammogram can be treated linearly.[23] However, some electrolytes approach the limits of our transient CV method and are likely in quasi-reversible kinetic regimes, as opposed to purely irreversible regimes. $j_0^{c.t.}$ is measured from the low overpotential slope of the cyclic voltammetry experiment as shown in Figure 1G, and the reported values are always the average of at least three measurements. Representative voltammograms are reported in Figure S2, and new data are tabulated in Figure S3.

Electrochemical Impedance Spectroscopy. Symmetric Li||Li 2032-type coin cells were used to measure R_{SEI} in each electrolyte. The cells were prepared in an argon-filled glovebox (Vigor, oxygen <1 ppm, water <0.1 ppm). Each cell used two polished and flattened 1 cm^2 discs of Li, 60 μL of electrolyte, and a 25 μm-thick polypropylene−polyethylene−polypropylene separator (Celgard). A 16-channel electrochemical workstation (VMP3, Biologic Science Instruments) was used. Since the SEI grows with time and R_{SEI} depends on the thickness and resistivity of the SEI,[9] R_{SEI} was measured at an OCV immediately after cell assembly (about 5 min after contact with the electrolyte). A frequency range of 1 MHz to 0.2 Hz was used with a perturbation amplitude of 5 mV. Each spectrum showed the characteristic depressed semicircle associated with the impedance of Li metal in non-aqueous electrolytes. To calculate R_{SEI}, the raw data was averaged between the two equivalent Li electrodes (divided by 2) and normalized to the surface area of one Li electrode (1 cm^2). The *Z*-fit EIS fitting software from EC-Lab was used to fit the spectrum to an equivalent circuit verified to describe the SEI (Figure S1). Only data with a frequency >20 Hz was included for the fit.[24]

CE Measurements. Cycling measurements were made with an Arbin battery cycler. Type 2032 coin cells with a Li foil (1 cm,[2] Alfa) counter electrode and a Cu working electrode (Pred Materials). Prior to cycling, the cells were held at 0 V for 24 h to preform SEI on Cu and reduce residual CuO. The cells were then cycled at a rate of 1 mA/cm^2 for both charge and discharge. A capacity cutoff of 1 mA h/cm^2 was used for charging (electroplating of Li) and a voltage cutoff of 1 V was used for discharging. The ratio of charge input during charge to charge output during discharge quantifies the CE.

Scanning Electron Microscopy. Samples for SEM analysis of the initial stages of nucleation were prepared in an argon-filled glovebox (Vigor, oxygen <1 ppm, water <0.1 ppm). 2032-type coin cells were used with 60 μL of electrolyte and a Li metal electrode as the counter/reference, a separator, and Cu foil as the working electrode (Pred Materials). Prior to electroplating of Li on Cu, the cells were held at 0 V to preform the SEI on Cu and make comparison of equivalent Li capacities in different electrolytes easier. Li was electrodeposited onto the Cu foil using an Arbin battery cycler with a rate of 1 mA/cm^2 and a cutoff capacity of 0.03 mA h/cm^2. Immediately following electroplating, cells were disassembled in the argon-filled glovebox, the freshly plated Li was rinsed with 20 μL of DEC to remove salts, and the samples were transferred immediately to SEM (FEI Magellan 400 XHR, 3 kV). The average particle size was measured using the SEM images as shown in Figures S6−S8. Samples for the SEM analysis of surface morphology during later stages of electroplating in Figure 1 were prepared identically except 1 mA h/cm^2 of Li was electrodeposited. To calculate the nucleation overpotential, a capacity of 0.003 mA h/cm^2 was used as the reference for the steady-state growth of Li as used in previous reports.[35,36] The capacity of 0.003 mA h/cm^2 was used, because it is the initial time where the voltage curves appear to taper off and achieve a steady state, preventing additional uncertainties from surface area changes.

Viscosity Measurement. Viscosities were assessed using an ARES G2 rheometer (TA Instruments) under ambient room-temperature conditions. To minimize the artifacts from exposure of the electrolytes to air, electrolytes were maintained in an argon atmosphere until immediately prior to each measurement.

Potentiometric Measurement. The relative free energies of solvation were measured using the design described in our previous work.[8] An H-cell using equivalent lithium electrodes but distinct asymmetric electrolytes is used to measure the free energy with respect to a reference 1 M LiFSI in DEC electrolyte. The free energy difference is measured with the cell voltage (Biologic VMP3) using the Nernst equation $\Delta G = -nFE$, where n is 1 for the $Li^+ + e^- \rightarrow Li$ reaction, F is the Faraday constant, E is the cell voltage, and ΔG is the free energy difference of Li^+ in distinct electrolytes relative to 1 M LiFSI in DEC electrolyte. Voltages were recorded as a function of time, and once the voltage stabilized over about 3 min, the cell voltage was used to calculate ΔG. The difference in free energy represents the difference in the chemical potential of Li^+ in distinct electrolytes relative to 1 M LiFSI in DEC electrolyte. To minimize the artifacts from a liquid junction potential between the two electrolytes, a salt bridge containing LiTFSI, where the transference numbers are 0.5, are used. At least three independent measurements are used.

Preparation of Electrolytes. All electrolytes were prepared and handled in an argon-filled glovebox (Vigor, oxygen <1 ppm, water <0.1 ppm). The 1 M $LiPF_6$ in EC/DEC electrolyte was used as received from Gotion. LiFSI (Oakwood) was dried for 24 h prior to dissolving into all LiFSI-containing solvents. Other EC/DEC electrolytes were prepared with a 1:1 v/v mixture of EC (99+%, Acros) and DEC (>99% anhydrous, Aldrich) with 1 M $LiClO_4$ (99+% anhydrous, Acros Organics), $LiAsF_6$ (99% Alfa Aesar), LiI (99.9% trace metals basis Aldrich), LiTFSI (Solvay), or LiFSI (Oakwood). The PC and DEC electrolytes contained 1 M $LiPF_6$ (99.99% battery grade, Aldrich) in PC (99.5% Extra dry Acros) and DEC (>99% anhydrous, Aldrich), respectively. The 1,2-dimethoxyethane (DME) electrolyte was a 1 M solution of LiFSI (Oakwood) in DME (Aldrich). Other solvents such as DME (Sigma, anhydrous, 99.5%) and 2,2,3,3-tetrafluoropropyl ether (TTE, Synquest) were used as received. Fluorinated dimethyl butane, fluorinated diethyl butane, and F5DEE were synthesized as reported previously.[3] 1,2-Diethoxyethane was used as received (99%, ACROS). LiTFSI [1,3-dioxolane (DOL):DME] with $LiNO_3$ was prepared with LiTFSI (Solvay), a 1:1 mixture of DME and DOL (Aldrich) and 2.5% by weight $LiNO_3$ (Aldrich). The EC/DEC electrolyte with 10% FEC electrolyte was prepared by adding 10% by volume of FEC (BASF) to the Gotion LP 40 electrolyte. FEC (BASF) was also used for 1 M LiFSI in FEC

https://doi.org/10.1021/jacs.2c08182
J. Am. Chem. Soc. 2022, 144, 20717−20725

electrolyte and 0.6 M lithium difluoro difluoro(oxalato)borate (LiDFOB) and 0.6 M $LiBF_4$ electrolyte.

■ ASSOCIATED CONTENT

Supporting Information

The Supporting Information is available free of charge at https://pubs.acs.org/doi/10.1021/jacs.2c08182.

Nyquist plots and voltammograms, tabulated data, fits from EIS and transient CV measurements, and additional digital and SEM images used for measuring the size of Li particles in different electrolytes (PDF)

■ AUTHOR INFORMATION

Corresponding Authors

Zhenan Bao − *Department of Chemical Engineering, Stanford University, Stanford, California 94305, United States;* orcid.org/0000-0002-0972-1715; Email: zbao@stanfod.edu

Yi Cui − *Department of Materials Science and Engineering, Stanford University, Stanford, California 94305, United States; Stanford Institute for Materials and Energy Sciences, SLAC National Accelerator Laboratory, Menlo Park, California 94025, United States;* orcid.org/0000-0002-6103-6352; Email: yicui@stanford.edu

Authors

David T. Boyle − *Department of Chemistry, Stanford University, Stanford, California 94305, United States;* orcid.org/0000-0002-0452-275X

Sang Cheol Kim − *Department of Materials Science and Engineering, Stanford University, Stanford, California 94305, United States;* orcid.org/0000-0002-1749-8277

Solomon T. Oyakhire − *Department of Chemical Engineering, Stanford University, Stanford, California 94305, United States;* orcid.org/0000-0002-3189-5949

Rafael A. Vilá − *Department of Materials Science and Engineering, Stanford University, Stanford, California 94305, United States*

Zhuojun Huang − *Department of Materials Science and Engineering and Department of Chemical Engineering, Stanford University, Stanford, California 94305, United States;* orcid.org/0000-0001-6236-8693

Philaphon Sayavong − *Department of Chemistry, Stanford University, Stanford, California 94305, United States*

Jian Qin − *Department of Chemical Engineering, Stanford University, Stanford, California 94305, United States;* orcid.org/0000-0001-6271-068X

Complete contact information is available at: https://pubs.acs.org/10.1021/jacs.2c08182

Notes

The authors declare no competing financial interest.

■ ACKNOWLEDGMENTS

We acknowledge the support from the Assistant Secretary for Energy Efficiency and Renewable Energy, Office of Vehicle Technologies of the US Department of Energy under the Battery Materials Research (BMR) Program and Battery 500 Consortium. D.T.B. and R.A.V acknowledge the support from the National Science Foundation Graduate Research Fellowship Program. S.T.O. acknowledges the support from the Knight Hennessy Fellowship. SEM was performed at the Stanford Nano Shared Facilities (SNSF), partially supported by the National Science Foundation under award ECCS-1542152.

■ REFERENCES

(1) Viswanathan, V.; Epstein, A. H.; Chiang, Y.-M.; Takeuchi, E.; Bradley, M.; Langford, J.; Winter, M. The Challenges and Opportunities of Battery-Powered Flight. *Nature* **2022**, *601*, 519−525.

(2) Xiao, J.; Li, Q.; Bi, Y.; Cai, M.; Dunn, B.; Glossmann, T.; Liu, J.; Osaka, T.; Sugiura, R.; Wu, B.; et al. Understanding and Applying Coulombic Efficiency in Lithium Metal Batteries. *Nat. Energy* **2020**, *5*, 561−568.

(3) Yu, Z.; Rudnicki, P. E.; Zhang, Z.; Huang, Z.; Celik, H.; Oyakhire, S. T.; Chen, Y.; Kong, X.; Kim, S. C.; Xiao, X.; et al. Rational Solvent Molecule Tuning for High-Performance Lithium Metal Battery Electrolytes. *Nat. Energy* **2022**, *7*, 94−106.

(4) Cao, X.; Ren, X.; Zou, L.; Engelhard, M. H.; Huang, W.; Wang, H.; Matthews, B. E.; Lee, H.; Niu, C.; Arey, B. W.; et al. Monolithic Solid−Electrolyte Interphases Formed in Fluorinated Orthoformate-Based Electrolytes Minimize Li Depletion and Pulverization. *Nat. Energy* **2019**, *4*, 796−805.

(5) Louli, A. J.; Eldesoky, A.; Weber, R.; Genovese, M.; Coon, M.; deGooyer, J.; Deng, Z.; White, R. T.; Lee, J.; Rodgers, T.; et al. Diagnosing and Correcting Anode-Free Cell Failure via Electrolyte and Morphological Analysis. *Nat. Energy* **2020**, *5*, 693−702.

(6) Hobold, G. M.; Lopez, J.; Guo, R.; Minafra, N.; Banerjee, A.; Meng, Y. S.; Shao-horn, Y.; Gallant, B. M. Moving beyond 99.9% Coulombic Efficiency for Lithium Anodes in Liquid Electrolytes. *Nat. Energy* **2021**, *6*, 951−960.

(7) Fan, X.; Ji, X.; Chen, L.; Chen, J.; Deng, T.; Han, F.; Yue, J.; Piao, N.; Wang, R.; Zhou, X.; et al. All-Temperature Batteries Enabled by Fluorinated Electrolytes with Non-Polar Solvents. *Nat. Energy* **2019**, *4*, 882.

(8) Kim, S. C.; Kong, X.; Vilá, R. A.; Huang, W.; Chen, Y.; Boyle, D. T.; Yu, Z.; Wang, H.; Bao, Z.; Qin, J.; et al. Potentiometric Measurement to Probe Solvation Energy and Its Correlation to Lithium Battery Cyclability. *J. Am. Chem. Soc.* **2021**, *143*, 10301−10308.

(9) Boyle, D. T.; Huang, W.; Wang, H.; Li, Y.; Chen, H.; Yu, Z.; Zhang, W.; Bao, Z.; Cui, Y. Corrosion of Lithium Metal Anodes during Calendar Ageing and Its Microscopic Origins. *Nat. Energy* **2021**, *6*, 487−494.

(10) Fang, C.; Li, J.; Zhang, M.; Zhang, Y.; Yang, F.; Lee, J. Z.; Lee, M.; Alvarado, J.; Schroeder, M. A.; Yang, Y.; et al. Quantifying Inactive Lithium in Lithium Metal Batteries. *Nature* **2019**, *572*, 511−515.

(11) *Modern Electroplating*, 5th ed.; Schlesinger, M., Paunovic, M., Eds.; John Wiley & Sons, Inc: Hoboken, New Jersey, 2010.

(12) Popov, K. I.; Djoki, S. S.; Jovi, V. D.*Morphology of Electrochemically and Chemically Deposited Metals*; Springer Nature, 2016.

(13) Liu, Y.; Xu, X.; Sadd, M.; Kapitanova, O. O.; Krivchenko, V. A.; Ban, J.; Wang, J.; Jiao, X.; Song, Z.; Song, J.; et al. Insight into the Critical Role of Exchange Current Density on Electrodeposition Behavior of Lithium Metal. *Adv. Sci.* **2021**, *8*, 2003301.

(14) Chen, X. R.; Yao, Y. X.; Yan, C.; Zhang, R.; Cheng, X. B.; Zhang, Q. A Diffusion–Reaction Competition Mechanism to Tailor Lithium Deposition for Lithium-Metal Batteries. *Angew. Chem., Int. Ed.* **2020**, *59*, 7743−7747.

(15) Liu, Z.; Li, Y.; Ji, Y.; Zhang, Q.; Xiao, X.; Yao, Y.; Chen, L. Q.; Qi, Y. Dendrite-Free Lithium Based on Lessons Learned from Lithium and Magnesium Electrodeposition Morphology Simulations. *Cell Rep. Phys. Sci.* **2021**, *2*, 100294.

(16) May, R.; Fritzsching, K. J.; Livitz, D.; Denny, S. R.; Marbella, L. E. Rapid Interfacial Exchange of Li Ions Dictates High Coulombic Efficiency in Li Metal Anodes. *ACS Energy Lett.* **2021**, *6*, 1162−1169.

(17) Liu, Y.; Lin, D.; Li, Y.; Chen, G.; Pei, A.; Nix, O.; Li, Y.; Cui, Y. Solubility-Mediated Sustained Release Enabling Nitrate Additive in Carbonate Electrolytes for Stable Lithium Metal Anode. *Nat. Commun.* **2018**, *9*, 3656.
(18) Zhang, X.-Q.; Chen, X.; Hou, L.-P.; Li, B.-Q.; Cheng, X.-B.; Huang, J.-Q.; Zhang, Q. Regulating Anions in the Solvation Sheath of Lithium Ions for Stable Lithium Metal Batteries. *ACS Energy Lett.* **2019**, *4*, 411−416.
(19) Zhao, Q.; Tu, Z.; Wei, S.; Zhang, K.; Choudhury, S.; Liu, X.; Archer, L. A. Building Organic/Inorganic Hybrid Interphases for Fast Interfacial Transport in Rechargeable Metal Batteries. *Angew. Chem., Int. Ed.* **2018**, *57*, 992−996.
(20) Su, C. C.; He, M.; Shi, J.; Amine, R.; Zhang, J.; Amine, K. Solvation Rule for Solid-Electrolyte Interphase Enabler in Lithium-Metal Batteries. *Angew. Chem., Int. Ed.* **2020**, *59*, 18229−18233.
(21) Peled, E.; Menkin, S. Review—SEI: Past, Present and Future. *J. Electrochem. Soc.* **2017**, *164*, A1703−A1719.
(22) Wu, H.; Jia, H.; Wang, C.; Zhang, J.; Xu, W. Recent Progress in Understanding Solid Electrolyte Interphase on Lithium Metal Anodes. *Adv. Energy Mater.* **2021**, *11*, 2003092.
(23) Boyle, D. T.; Kong, X.; Pei, A.; Rudnicki, P. E.; Shi, F.; Huang, W.; Bao, Z.; Qin, J.; Cui, Y. Transient Voltammetry with Ultramicroelectrodes Reveals the Electron Transfer Kinetics of Lithium Metal Anodes. *ACS Energy Lett.* **2020**, *5*, 701−709.
(24) Boyle, D. T.; Li, Y.; Pei, A.; Vila, R. A.; Sayavong, P.; Huang, W.; Zhang, Z.; Wang, H.; Liu, Y.; Xu, R.; et al. Resolving Current-dependent Regimes of Electroplating For Fast-Charging Lithium Metal Anodes. *Nano Lett.* **2022**, DOI: 10.1021/acs.nanolett.2c02792.
(25) Hobold, G. M.; Kim, K.-H.; Gallant, B. M. Beneficial vs Inhibiting Passivation by the Native Lithium Solid Electrolyte Interphase Revealed by Electrochemical Li^+ Exchange. *ChemRxiv* **2022**, 1−27.
(26) Hao, F.; Verma, A.; Mukherjee, P. P. Mesoscale Complexations in Lithium Electrodeposition. *ACS Appl. Mater. Interfaces* **2018**, *10*, 26320−26327.
(27) Xiao, J. How Lithium Dendrites Form in Liquid Batteries. *Science* **2019**, *366*, 426−427.
(28) Bard, A. J.; Faulkner, L. R.*Fundamentals and Applications*; John Wiley and Sons, Inc.: New Jersey, 2001.
(29) Yu, Z.; Wang, H.; Kong, X.; Huang, W.; Tsao, Y.; Mackanic, D. G.; Wang, K.; Wang, X.; Huang, W.; Choudhury, S.; et al. Molecular Design for Electrolyte Solvents Enabling Energy-Dense and Long-Cycling Lithium Metal Batteries. *Nat. Energy* **2020**, *5*, 526−533.
(30) Jurng, S.; Brown, Z. L.; Kim, J.; Lucht, B. L. Effect of Electrolyte on the Nanostructure of the Solid Electrolyte Interphase (SEI) and Performance of Lithium Metal Anodes. *Energy Environ. Sci.* **2018**, *11*, 2600−2608.
(31) Zhang, Y.; Viswanathan, V. Not All Fluorination Is the Same : Unique Effects of Fluorine Functionalization of Ethylene Carbonate for Tuning Solid-Electrolyte Interphase in Li Metal Batteries. *Langmuir* **2020**, *36*, 11450−11466.
(32) He, M.; Guo, R.; Hobold, G. M.; Gao, H.; Gallant, B. M. The Intrinsic Behavior of Lithium Fluoride in Solid Electrolyte Interphases on Lithium. *Proc. Natl. Acad. Sci. U.S.A.* **2020**, *117*, 73−79.
(33) Santos, E.; Schmickler, W. The Crucial Role of Local Excess Charges in Dendrite Growth on Lithium Electrodes. *Angew. Chem., Int. Ed.* **2021**, *60*, 5876−5881.
(34) Hagopian, A.; Doublet, M. L.; Filhol, J. S. Thermodynamic Origin of Dendrite Growth in Metal Anode Batteries. *Energy Environ. Sci.* **2020**, *13*, 5186−5197.
(35) Pei, A.; Zheng, G.; Shi, F.; Li, Y.; Cui, Y. Nanoscale Nucleation and Growth of Electrodeposited Lithium Metal. *Nano Lett.* **2017**, *17*, 1132−1139.
(36) Biswal, P.; Stalin, S.; Kludze, A.; Choudhury, S.; Archer, L. A. Nucleation and Early Stage Growth of Li Electrodeposits. *Nano Lett.* **2019**, *19*, 8191−8200.
(37) Liu, S.; Ji, X.; Yue, J.; Hou, S.; Wang, P.; Cui, C.; Chen, J.; Shao, B.; Li, J.; Han, F.; et al. High Interfacial-Energy Interphase Promoting Safe Lithium Metal Batteries. *J. Am. Chem. Soc.* **2020**, *142*, 2438−2447.
(38) Pinto, L. M. C.; Spohr, E.; Quaino, P.; Santos, E.; Schmickler, W. Why Silver Deposition Is so Fast: Solving the Enigma of Metal Deposition. *Angew. Chem., Int. Ed.* **2013**, *52*, 7883−7885.
(39) Fraggedakis, D.; McEldrew, M.; Smith, R. B.; Krishnan, Y.; Zhang, Y.; Bai, P.; Chueh, W. C.; Shao-Horn, Y.; Bazant, M. Z. Theory of Coupled Ion-Electron Transfer Kinetics. *Electrochim. Acta* **2021**, *367*, 137432.
(40) Lam, Y.; Soudackov, A. V.; Goldsmith, Z. K.; Hammes-Schiffer, S. Theory of Proton Discharge on Metal Electrodes : Electronically Adiabatic Model. *J. Phys. Chem. C* **2019**, *123*, 12335−12345.
(41) Mozhzhukhina, N.; Flores, E.; Lundström, R.; Nyström, V.; Kitz, P. G.; Edström, K.; Berg, E. J. Direct Operando Observation of Double Layer Charging and Early Solid Electrolyte Interphase Formation in Li-Ion Battery Electrolytes. *J. Phys. Chem. Lett.* **2020**, *11*, 4119−4123.
(42) Vatamanu, J.; Borodin, O.; Smith, G. D. Molecular Dynamics Simulation Studies of the Structure of a Mixed Carbonate/LiPF 6 Electrolyte near Graphite Surface as a Function of Electrode Potential. *J. Phys. Chem. C* **2012**, *116*, 1114−1121.
(43) Wen, B.; Deng, Z.; Tsai, P. C.; Lebens-Higgins, Z. W.; Piper, L. F. J.; Ong, S. P.; Chiang, Y. M. Ultrafast Ion Transport at a Cathode−Electrolyte Interface and Its Strong Dependence on Salt Solvation. *Nat. Energy* **2020**, *5*, 578−586.
(44) Park, J.; Zhao, H.; Kang, S. D.; Lim, K.; Chen, C. C.; Yu, Y. S.; Braatz, R. D.; Shapiro, D. A.; Hong, J.; Toney, M. F.; et al. Fictitious Phase Separation in Li Layered Oxides Driven by Electro-Autocatalysis. *Nat. Mater.* **2021**, *20*, 991−999.